Geophysical Research Letters

RESEARCH LETTER
10.1029/2020GL087222

Key Points:
- Joint inversion of daily and long-period geomagnetic variations results in better resolved mantle conductivity structure
- Incorporation of seismic constraints helps isolate mantle water content
- We find a relatively dry mantle beneath Europe and a water-enriched transition zone underneath North America and northern Asia

Supporting Information:
- Supporting Information S1

Correspondence to:
F. D. Munch,
fmunch@seismo.berkeley.edu

Citation:
Munch, F. D., Grayver, A. V., Guzavina, M., Kuvshinov, A. V., & Khan, A. (2020). Joint inversion of daily and long-period geomagnetic transfer functions reveals lateral variations in mantle water content. *Geophysical Research Letters*, *47*, e2020GL087222. https://doi.org/10.1029/2020GL087222

Received 30 JAN 2020
Accepted 11 APR 2020
Accepted article online 17 APR 2020

Joint Inversion of Daily and Long-Period Geomagnetic Transfer Functions Reveals Lateral Variations in Mantle Water Content

F. D. Munch[1], A. V. Grayver[1], M. Guzavina[1], A. V. Kuvshinov[1], and A. Khan[1,2]

[1]Institute of Geophysics, ETH Zürich, Zürich, Switzerland, [2]Institute of Theoretical Physics, University of Zürich, Zürich, Switzerland

Abstract We present a novel approach to investigate variations in upper mantle and transition zone (MTZ) water content based on the joint analysis of electromagnetic (EM) signals originating in the ionosphere and magnetosphere. We invert EM signals (period range 6 hr to 85 days) to probe the electrical conductivity structure underneath 20 geomagnetic observatories, accounting for the complex spatial structure of the ionospheric and magnetospheric sources. The joint inversion of EM data for the daily and long-period bands leads to significantly improved resolution in the upper mantle and MTZ. The conductivity profiles reveal significant lateral variability, which we interpret in terms of mantle water content by coupling electrical conductivity with constrains on mantle thermochemical structure derived from the analysis of seismic data. Our results suggest the existence of a relatively dry MTZ beneath Europe and a water-enriched MTZ underneath North America and northern Asia.

Plain Language Summary The amount of water trapped in the Earth's interior has a strong effect on the evolution and dynamics of the planet, which ultimately controls the occurrence of earthquakes and volcanic eruptions. However, the distribution of water inside the Earth is not yet well understood. To study the Earth's deep interior, we make use of changes in the Earth's magnetic field to detect variations in electrical conductivity inside the planet. Electrical conductivity is a characteristic of a rock that varies with temperature and water content. Here, we present a novel methodology to estimate the amount of water in different regions of Earth's mantle. Our analysis suggests the presence of small amounts of water in the mantle underneath Europe, whereas larger amounts are expected beneath North America and northern Asia.

1. Introduction

Constraining the water (hydrogen) distribution in Earth's interior is important for understanding its evolution and dynamics since water has a profound effect on rheological properties and melting relationships (e.g., Hirschmann, 2006; Karato, 2011). High-pressure mineral-physics studies have reported that mantle transition zone (MTZ) minerals can store large amounts of water (~1–3 wt%), whereas much smaller amounts (~0.1–0.2 wt%) can be stored in upper mantle minerals (e.g., Bolfan-Casanova, 2005; Hirschmann et al., 2005). Supporting evidence for a relatively dry (~0.02 wt%) upper mantle and a hydrous (~1 wt%) MTZ has been provided by the analysis of mantle xenoliths (e.g., Peslier et al., 2010; Peslier & Bizimis, 2015) and ringwoodite inclusions found in a natural diamond that truly originated in the MTZ (Pearson et al., 2014), respectively. However, the present distribution of water in the Earth's interior and the mechanisms for water exchange between different mantle reservoirs remain uncertain (e.g., Bolfan-Casanova et al., 2006; Hirschmann, 2006; Ohtani et al., 2004).

As electrical conductivity is a transport property that is highly sensitive to mantle temperature and the presence of water and melt (e.g., Karato, 2011; Katsura & Yoshino, 2015; Khan, 2016), deep electromagnetic (EM) sounding techniques play a fundamental role in mapping the distribution of water in the mantle by imaging variations in electrical conductivity (e.g., Kelbert et al., 2009; Koyama et al., 2014, 2006; Semenov & Kuvshinov, 2012; Shimizu et al., 2010; Sun et al., 2015). These techniques rely on the fact that primary magnetic fields (e.g., those that originate in the magnetosphere) penetrate into the deep Earth and induce secondary signals by virtue of EM induction. EM variations in the daily band (4–24 hr) are mainly dominated by the ionospheric current system, while variations with periods longer than 1 day are generated by

magnetospheric currents (e.g., Finlay et al., 2017). As penetration depth depends on frequency, analyzing these signals in as wide a range of periods as possible allows us to sense electrical conductivity variations in the widest depth range possible (e.g., Püthe et al., 2015a). However, EM sounding studies often rely on single-source data analysis facing the problem of limited depth resolution due to a limited frequency range imposed by various source morphologies (cf. Kuvshinov, 2008).

Only a few studies have attempted to combine EM responses from different sources. For instance, Egbert and Booker (1992) and Bahr et al. (1993) combined signals from magnetospheric and ionospheric origin recorded at geomagnetic observatories to obtain regional conductivity models of the mantle underneath North America and Europe, respectively. These studies, however, invoked simplistic source assumptions, which is likely to increase the chance of introducing source related model biases. Alternatively, Olsen (1998) accounted for a more complex source geometry (in the period range 3–720 hr) by incorporating estimates of horizontal gradients of the horizontal magnetic field. Given that direct measurement of these gradients on a single site is challenging in practice, the author estimated gradients from horizontal magnetic field components measured at an array of nearby observatories, which is limited to regions with a dense network of geomagnetic observatories (e.g., Europe). More recently, Grayver et al. (2017) jointly inverted the magnetospheric global response and ocean tidal signals from satellite magnetic field measurements, yielding a consistent global conductivity model of the oceanic upper mantle and MTZ.

Here, we perform inversions of daily (6–24 hr) and long-period (3–85 days) local responses recorded at a series of geomagnetic observatories to infer lateral variations in upper mantle and MTZ conductivity structure and water content. To isolate the influence of water on electrical conductivity from thermal effects, we follow Khan (2016) and combine phase equilibrium calculations, laboratory-measured electrical conductivity of mantle minerals, and estimates of mantle temperature and major element chemistry derived from the analysis of short- and long-period seismic data using the results of Munch et al. (2020).

2. Methods

2.1. Multisource EM Global-to-Local Transfer Functions

Signals due to the magnetospheric currents dominate natural geomagnetic variations at periods longer than 1 day (cf. Finlay et al., 2017; Olsen & Stolle, 2017). The source of these signals is often described via a single—first zonal-spherical harmonic, leading to the widely used local C-response (Banks, 1969). This transfer function (TF) relates vertical and horizontal components of the magnetic variations at an observational site. However, it is known that the magnetospheric source has a more complex structure, especially during the main phase of geomagnetic storms (e.g., Balasis & Egbert, 2006; Daglis & Kozyra, 2002; Olsen & Kuvshinov, 2004), thus potentially introducing errors in the estimated responses, resulting in biases in the retrieved conductivity structure (e.g., Püthe et al., 2015b). Furthermore, geomagnetic field variations in the period range between a few hours and 1 day are dominated by the ionospheric current systems that are characterized by a more complex morphology (e.g., Yamazaki & Maute, 2017). This complexity invalidates simplistic source models that would allow the use of a TF similar to the C-response. To account for complex ionospheric and magnetospheric sources, we resort to an alternative set of global-to-local TFs, $T_n^m(\mathbf{r}_a, \omega)$, that relate the vertical component of the magnetic field $Z(\mathbf{r}_a, \omega)$ at an observation site $\mathbf{r}_a = (a, \theta, \varphi)$ to a set of global spherical harmonic expansion (SHE) coefficients, $\varepsilon_n^m(\omega)$, that describe the source structure (Püthe et al., 2015b)

$$Z(\mathbf{r}_a, \omega) = \sum_{n=1}^{N_\varepsilon} \sum_{m=-n}^{n} \varepsilon_n^m(\omega)\ T_n^m(\mathbf{r}_a, \omega), \tag{1}$$

where N_ε is the maximum (cutoff) degree for the external SHE coefficients, ω is the angular frequency, a denotes the Earth's mean radius, θ is the colatitude, and φ is the longitude.

The estimation of global-to-local TFs is a two-step procedure: (i) external SHE coefficients describing the source are determined from horizontal components of the magnetic field measured at a global network of geomagnetic observatories assuming an a priori three-dimensional (3-D) Earth model, which consists of a mantle with a one-dimensional (1-D) conductivity distribution overlaid by a laterally varying surface conductance layer; the latter approximates the nonuniform distribution of oceans and continents (see Appendix A for details on estimating "magnetospheric" source coefficients). (ii) TFs are estimated by relating the vertical component of the magnetic field measured at every site of interest with the source coefficients determined in the previous step. The data for estimating "magnetospheric" TFs consist of hourly

mean values of geomagnetic field variations measured at 132 mid-latitude (geomagnetic latitudes between ±6° and ±56°) permanent geomagnetic observatories (see Figure S1 in supporting information) for the years 1998–2018 retrieved from the British Geological Survey (BGS) database (Macmillan & Olsen, 2013). After removal of the main field and its secular variations using the CHAOS model (Olsen et al., 2006), source coefficients and global-to-local TFs for the long-period band (3–85 days) were determined following the procedures described in Püthe et al. (2015b), which includes section-averaging (e.g., Olsen, 1998) and Huber-weighted robust least squares methods (e.g., Aster et al., 2005). As for global-to-local TFs in the daily band (24, 12, 8, and 6 hr), we used those estimated by Guzavina et al. (2019) from the BGS database. Geographic and geomagnetic coordinate systems were used for estimating "daily" and "long-period" TFs, respectively.

2.2. Probabilistic Inversion

We employed the probabilistic approach of Tarantola and Valette (1982) and the Metropolis algorithm (e.g., Hastings, 1970; Metropolis et al., 1953) to determine the conductivity structure underneath each station from the estimated global-to-local TFs. Building on previous experience (Munch et al., 2018), we reduced the burn-in stage of the Metropolis algorithm by using a global optimization technique (Covariance Matrix Adaptation Evolution Strategy; Hansen & Ostermeier, 2001) to obtain a good initial model $\mathbf{m}_0$ for every inversion. The solution of the nonlinear inverse problem is then given in terms of the posterior probability distribution

$$\gamma(\mathbf{m}|\mathbf{d}) \propto \exp\left[-\frac{\phi(\mathbf{m},\mathbf{d})}{2}\right] \exp\left[-\frac{\beta}{p_m}\sum_{i=1}^{N}\left|\nabla \mathrm{m}_i\right|^{p_m}\right], \tag{2}$$

where $\mathbf{d}$ denotes observed data and $\mathbf{m} = [\lambda(\sigma_1) \ldots \lambda(\sigma_N)]$ represents the unknown conductivity structure, with $\lambda(\cdot)$ being a log-based transformation ensuring positivity of the argument. The subsurface was parameterized in terms of 25 layers ranging in thickness from 50 km in the upper mantle and MTZ to 400 km at the core-mantle boundary with a fixed core conductivity ($\sigma = 10^5$ S/m). The regularization parameter β was determined by means of an L-curve analysis (Hansen, 1999) performed on the models $\mathbf{m}_0$ and the scalar p_m was set to 1.5 which provides a good balance between sharp conductivity contrasts and smooth models (Grayver & Kuvshinov, 2016). The data misfit term is given by

$$\phi(\mathbf{m},\mathbf{d}) = \sum_{k\in\mathcal{M}}\left(\frac{1}{N_k}\sum_{i=1}^{N_k}\left|w_i^k\,(f_i^k(\mathbf{m}) - d_i^k)\right|^2\right), \tag{3}$$

where $\mathcal{M}$ denote the EM methods in the daily and long-period bands and w^k, $f^k(\mathbf{m})$, and d^k are corresponding data weights (reciprocal of uncertainties), forward operator, and observed data, respectively. As discussed by Grayver et al. (2017), normalizing with the number of actual measurements (N_k) is an important aspect that helps balance the contribution of each EM technique.

2.3. Inference of Water Content From Retrieved Conductivity Profiles

We interpreted the obtained conductivity profiles in terms of upper mantle and MTZ water content by comparing the retrieved models with laboratory-based conductivity profiles computed using the approach of Khan (2016). To isolate the influence of water on electrical conductivity from thermal effects, we constrained mantle temperature and major element chemistry underneath each geomagnetic observatory by incorporating into the inversion probability density functions independently derived from the inversion of short- (P-to-s receiver functions) and long-period (Rayleigh wave phase velocities) seismic data from a nearby seismic station (Munch et al., 2020). Mantle composition was parameterized in terms of a single variable that represents the amount of basalt in a basalt-harzburgite mixture, with the composition of basalt and harzburgite end-members described using the CFMASNa chemical model system comprising the oxides CaO-MgO-FeO-Al_2O_3-SiO_2-Na_2O. Mantle temperature was described in terms of an adiabat defined by the mantle potential temperature T_p, which represents the temperature that a parcel of the mantle would have at the surface, if it ascended along an adiabat without undergoing melting (McKenzie & Bickle, 1988).

The laboratory-based conductivity profiles were computed from mineral phase equilibrium calculations and experimental measurements of mantle mineral conductivities. We employed the Gibbs free-energy minimization strategy of Connolly (2009) and the self-consistent thermodynamic formulation of Stixrude and Lithgow-Bertelloni (2005) with parameters given by Stixrude and Lithgow-Bertelloni (2011) to predict stable mineralogy (mineral modes) as a function of pressure, temperature, and composition. Several independent

measurements of the electrical conductivity for major upper mantle and MTZ minerals exist. To minimize subjectivity, we here considered two databases built on the measurements of (i) Yoshino, Katsura, and coworkers (referred to as YK) and (ii) Karato, Dai, and coworkers (referred to as KD). Table S2 provides the list of data sources used to build the YK and KD databases. The laboratory-measured databases account for the effect of water content on the following hydrous minerals: olivine, orthopyroxene, clinopyroxene, wadsleyite, ringwoodite, and garnet (only KD database). Building on previous experience (e.g., Khan, 2016), we parameterized the water content of the mantle in terms of the water contents in olivine (upper mantle) and wadsleyite (transition zone). Water contents in orthopyroxene, clinopyroxene, and ringwoodite were estimated using the water partition coefficients based on measurements from Inoue et al. (2010) and Ferot and Bolfan-Casanova (2012). Water content in garnet (only relevant for KD database) was estimated using the water partition coefficients derived by Mookherjee and Karato (2010).

3. Results

3.1. Long-Period TFs

As discussed above, we estimated global-to-local TFs in the period range 3–85 days from 21 years (1998–2018) of ground-based geomagnetic observatory data. In order to better account for the complexity of the source, magnetospheric time series were parameterized in terms of 13 SHE coefficients ($\varepsilon_1^0, \varepsilon_1^1, \varepsilon_1^{-1}, \varepsilon_2^0, \varepsilon_2^1, \varepsilon_2^{-1}, \varepsilon_2^2, \varepsilon_2^{-2}, \varepsilon_3^2, \varepsilon_3^{-2}, \varepsilon_4^0, \varepsilon_4^1$, and ε_4^{-1}). The choice of source coefficients aims at maximizing the coefficient of determination (i.e., measure of how well a proposed source geometry predicts the observed time series; see Figure S2), while minimizing the number of source terms that limits the maximum period for which multivariate TFs can be estimated (Püthe & Kuvshinov, 2014) and that may result in overfitting. All source terms were used to estimate long-period global-to-local TFs T_n^m, but only the dominant source term T_1^0 was considered in the inversion to retrieve the conductivity structure underneath each station because this TF is most sensitive to the radial structure of the Earth (Kuvshinov, 2008). In the daily band, we also considered only TFs corresponding to dominant source terms, namely, T_p^{p+1} at periods $24/p$ hr (p = 1–4). As discussed in section 2.1, the estimation of source coefficients requires the assumption of a mantle 1-D conductivity profile to separate the external (inducing) from the internal (induced) contributions in the measured geomagnetic variations. We find that differences in the long-period TFs introduced by the choice of the mantle conductivity profile are within data uncertainties (see Figure S3).

Figure 1a depicts estimated long-period responses T_1^0, uncertainties, and squared coherencies (coh^2) for four geomagnetic observatories: Boulder (BOU, USA), Niemegk (NGK, Germany), Belsk (BEL, Poland), and Irkutsk (IRT, Russia). For comparison, TFs $\hat{T}_1^0$ estimated assuming that the source is described by the first zonal spherical harmonic are also shown. In this case, the TFs were derived from the local C-response $C(\mathbf{r}_a, \omega)$—estimated using the Z/H method of Banks (1969)—as $\hat{T}_1^0(\mathbf{r}_a, \omega) = \frac{3\, C(\mathbf{r}_a,\omega)}{C(\mathbf{r}_a,\omega)+a} \cos\theta$. In agreement with previous studies (Püthe et al., 2015b), we find that the incorporation of additional source terms increases the squared coherency, especially at periods <10 days and geomagnetic latitudes >40°, thus decreasing the potential bias of the responses that could result from correlated noise and spatial aliasing (Olsen, 1998). Figure 1b shows the average relative difference between T_1^0 and $\hat{T}_1^0$ as a function of geomagnetic colatitude. We observe that the use of simplistic source models results in significant differences of the estimated TFs, particularly for the imaginary part, which can potentially bias the inversion.

3.2. Data Fit and Recovered Conductivity Models

The TFs were individually inverted to determine the most probable set of conductivity profiles underneath 20 inland geomagnetic observatories (see Figure 2), for which synthetic TFs can be computed with low computational cost using analytical solutions for radial 1-D Earth models. Coastal and island geomagnetic observatories have been excluded from this analysis because calculation of synthetic TFs for these locations requires the use of 3-D solvers to account for ocean induction effects (e.g., Kuvshinov et al., 2002), making the use of Markov chain Monte Carlo methods (e.g., Mosegaard & Tarantola, 1995) impracticable.

We succeed at explaining the observed daily and long-period EM variations for 13 geomagnetic observatories (see Figures S5–S7), indicated in Figure 2 by red stars surrounded by black circles. However, we find a cluster of seven stations located in Europe (black circles in Figure 2) for which the fit of daily TFs is unsatisfactory under the 1-D assumption (see Figures S5–S7). One can speculate that this reflects (1) the presence of anomalously shallow 3-D structure underneath central Europe and the Mediterranean linked to the subduction and ponding of slabs in the MTZ as suggested by seismic tomography (e.g., Cottaar & Deuss, 2016;

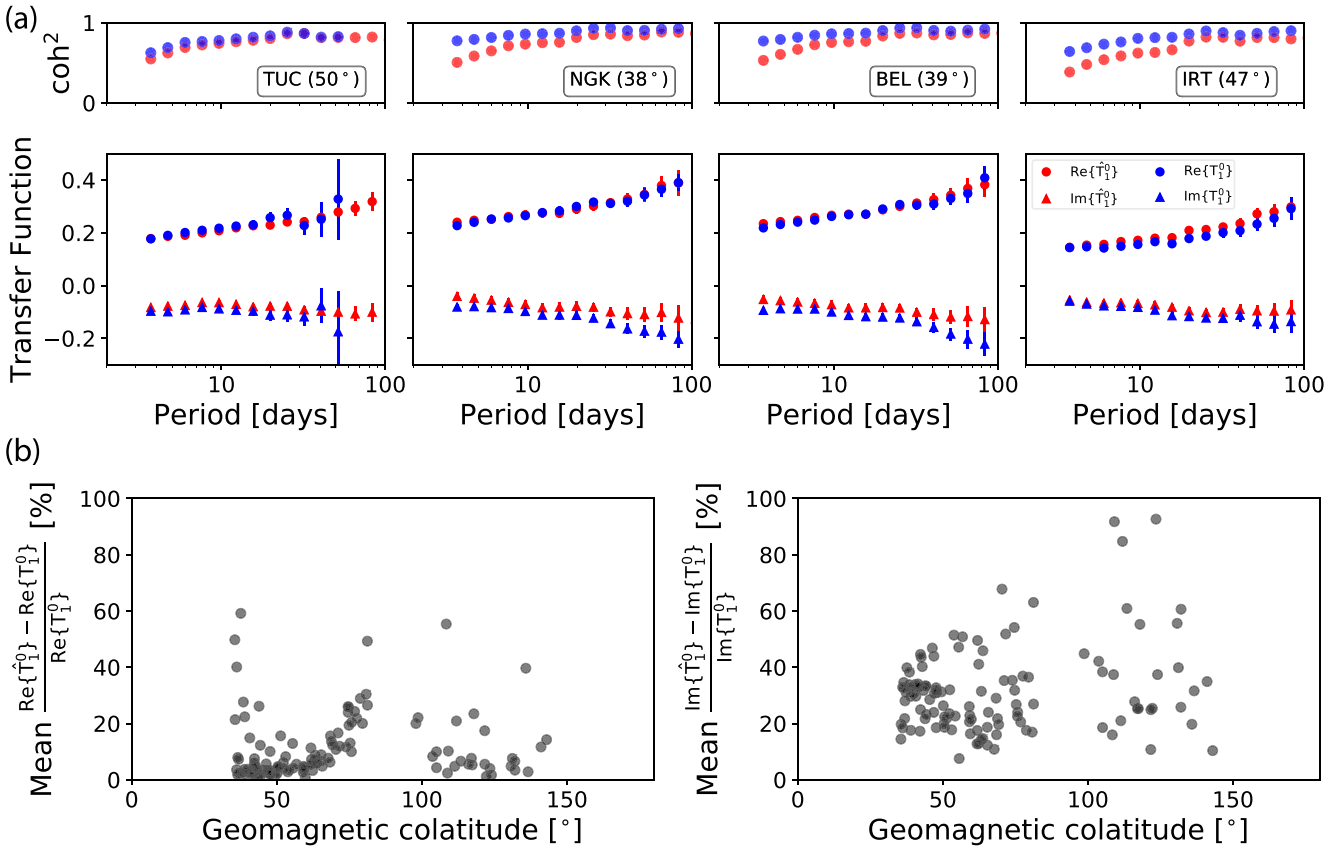

Figure 1. Example of experimental global-to-local transfer functions. (a) Real (positive) and imaginary (negative) parts of the experimental global-to-local (blue) transfer functions T_1^0 (bottom row) and squared coherencies coh^2 (top row) estimated in this study for Boulder (BOU), Niemegk (NGK), Belsk (BEL), and Irkutsk (IRT) geomagnetic observatories. Geographic location of the geomagnetic observatories are shown in Figure 2. Error bars indicate uncertainties of the experimental transfer functions. For comparison, transfer functions $\hat{T}_1^0$ obtained for a case when the source is described by the first zonal spherical harmonic are shown in red. (b) Mean relative differences between the real (left) and imaginary (right) parts of T_1^0 and $\hat{T}_1^0$ as a function of geomagnetic colatitude.

Zhu et al., 2015) or (2) artifacts due to the presence of noise (e.g., signals due to polar eletrojet currents) that are not accounted for in the presently used source parameterization.

Figure S4 illustrates the posterior probability distributions obtained when inverting daily and long-period signals separately and jointly at a single station (Alice Spring in Australia). In agreement with previous studies (e.g., Munch et al., 2018), long-period signals best constrain the conductivity structure in the depth range between 400 and 1,400 km (see Figure S4b), while daily variations provide information on the conductivity structure between 200- and 500-km depth (see Figure S4a) (e.g., Koch & Kuvshinov, 2013). The models obtained from the joint inversion of daily and long-period signals (see Figure S4c) manage to resolve the conductivity structure in the upper mantle (200- to 400-km depth), MTZ (400- to 660-km depth), and the uppermost lower mantle (660- to 1,400-km depth).

3.3. Constraints on Upper Mantle and MTZ Water Content

We determined the range of water contents in olivine and wadsleyite that best explain the inverted conductivity profiles between 200- and 1,200-km depth. This was achieved by comparing the inverted conductivity models with laboratory-based conductivity profiles (described in section 2.3) using an L_2-norm misfit function and the Metropolis algorithm. In particular, we focus on eight geomagnetic observatories for which probability density functions of the mantle potential temperature and composition (basalt fraction) derived from the inversion of short- and long-period seismic data (Munch et al., 2020) recorded at a nearby station (indicated by triangles in Figure 2) are available.

Figure 3 summarizes the conductivity models obtained from the joint inversion of long-period and daily signals (black) and best-fitting laboratory-based conductivity profiles (green). Laboratory-based conductivity profiles implicitly incorporate discontinuities across the major phase transitions (olivine→ wadsleyite,

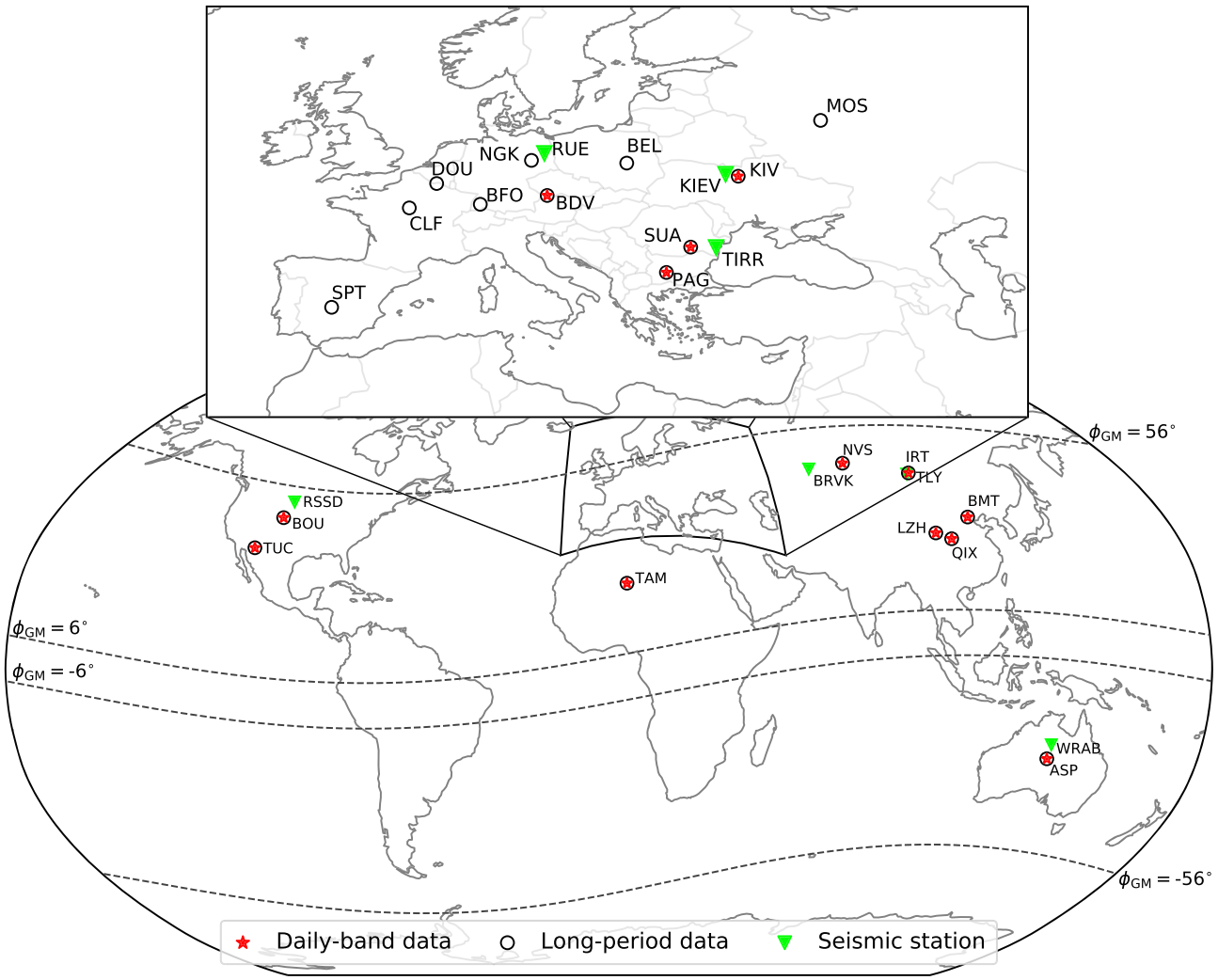

Figure 2. Geographic location of mid-latitude observatories used in this study between geomagnetic latitudes ϕ_{GM} −56° to −6° and 6°–56°. Red stars and black circles denote stations at which the observed daily (6–24 hr) and long-period (3–85 days) transfer functions are successfully fitted in the inversion, respectively. Green triangles indicate seismic stations for which constraints on mantle temperature and composition were derived by Munch et al. (2020) from analysis of short- and long-period seismic data. Station information is summarized in Table S1. Data fit for all stations is shown in Figures S5–S7.

wadsleyite→ ringwoodite, and ringwoodite→ bridgmanite + ferropericlase), whereas the conductivity models retrieved from the inversion of observed EM responses are smoother down to depths of ~1,000 km. We find an overall agreement between the inverted conductivity models and laboratory-based conductivity profiles particularly in the upper mantle and MTZ. However, we observe that laboratory-based conductivity profiles are systematically more conductive in the lower mantle (800–1,200-km depth) than the conductivity models derived from the observed data. This difference might reflect that (1) temperature estimates derived from the inversion of seismic data might be biased toward higher temperatures or (2) the laboratory-based conductivity databases considered in this work tend to overestimate the electrical conductivity of lower-mantle minerals. Future work should aim at refining the laboratory-based mineral conductivity databases, particularly for lower-mantle minerals, as the degree to which hydrogen affects the electrical conductivity of lower-mantle minerals remains uncertain. In this light, determining the influence of hydrogen on electrical conductivity in the lower-mantle minerals is critical to improve the current understanding of the water distribution in the deep mantle and the circulation between the various reservoirs.

Figure 4 depicts inferences on water content in the upper mantle and MTZ minerals olivine (C_w^{ol}) and wadsleyite (C_w^{wad}) obtained using the YK and KD databases. The former database generally leads to a significantly

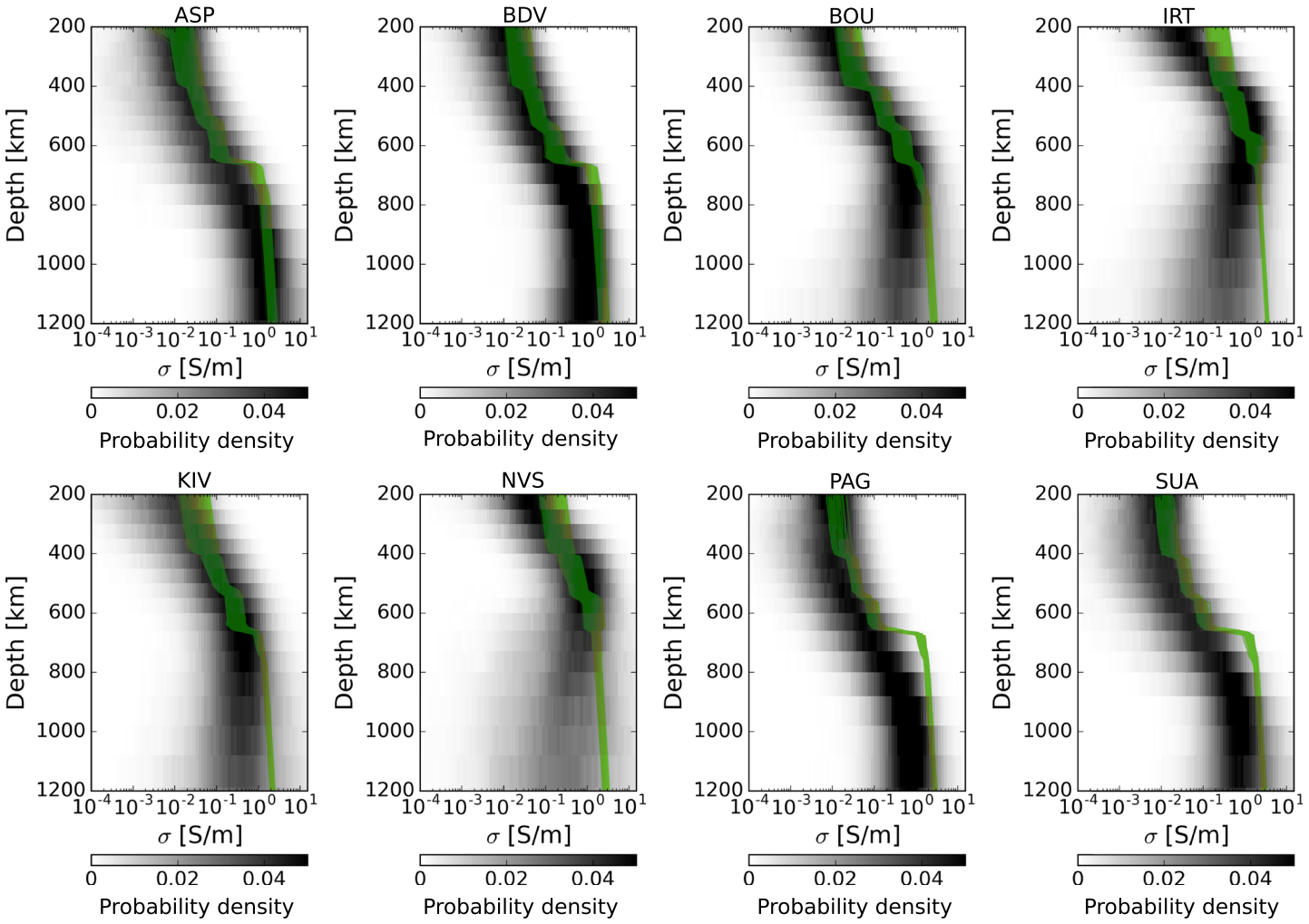

Figure 3. Posterior probability distributions of electrical conductivity (σ) retrieved from the joint inversion of daily and long-period transfer functions (black) and best-fitting laboratory-based conductivity profiles (green) for the Karato-Dai (KD) database. The geographic location of each geomagnetic observatory is shown in Figure 2, and station acronyms are defined in Table S1. Best-fitting laboratory-based conductivity profiles obtained using the Yoshino-Katsura (YK) database are shown in Figure S8.

more hydrated upper mantle and MTZ. As discussed by Khan and Shankland (2012), this difference arises from the fact that the KD database tends to result in higher electrical conductivities for a given water content. The use of the YK database results in anomalously high water contents ($C_w^{ol} \sim 0.3$ wt% and $C_w^{wad} \sim 1.9$ wt%) underneath stations located in northern Asia (NVS and IRT). These estimates significantly exceed the experimentally determined water storage capacity of mantle minerals (e.g., Hirschmann et al., 2005; Litasov et al., 2011), which would result in the accumulation of partial melt atop the MTZ (Bercovici & Karato, 2003). However, no evidence for the existence of a melt layer (i.e., negative amplitudes on the receiver function waveforms due to a low shear-wave velocity anomaly) is observed in the seismic data, and further analysis focuses on estimates derived with the KD database.

In agreement with previous studies (e.g., Fullea et al., 2011; Jones et al., 2012; Karato, 2011; Khan & Shankland, 2012), our results indicate a relatively dry upper mantle ($C_w^{ol} < 0.02$ wt%) underneath all stations, whereas significat lateral variability in MTZ water content is observed. We find relatively low MTZ water contents ($C_w^{wad} < 0.05$ wt%) in Australia (ASP) and Europe (BDV, PAG, SUA, and KIV), whereas moderate ($C_w^{wad} \sim 0.15$ wt%) and high water contents ($C_w^{wad} \sim 0.3$ wt%) are required to explain the inverted conductivity profiles in Asia (IRT and NVS) and North America (BOU), respectively. A dry MTZ below Europe has already been suggested by Utada et al. (2009) from the joint analysis of seismic and EM models. In agreement with MTZ water contents experimentally determined by Freitas et al. (2017), our estimates suggest that

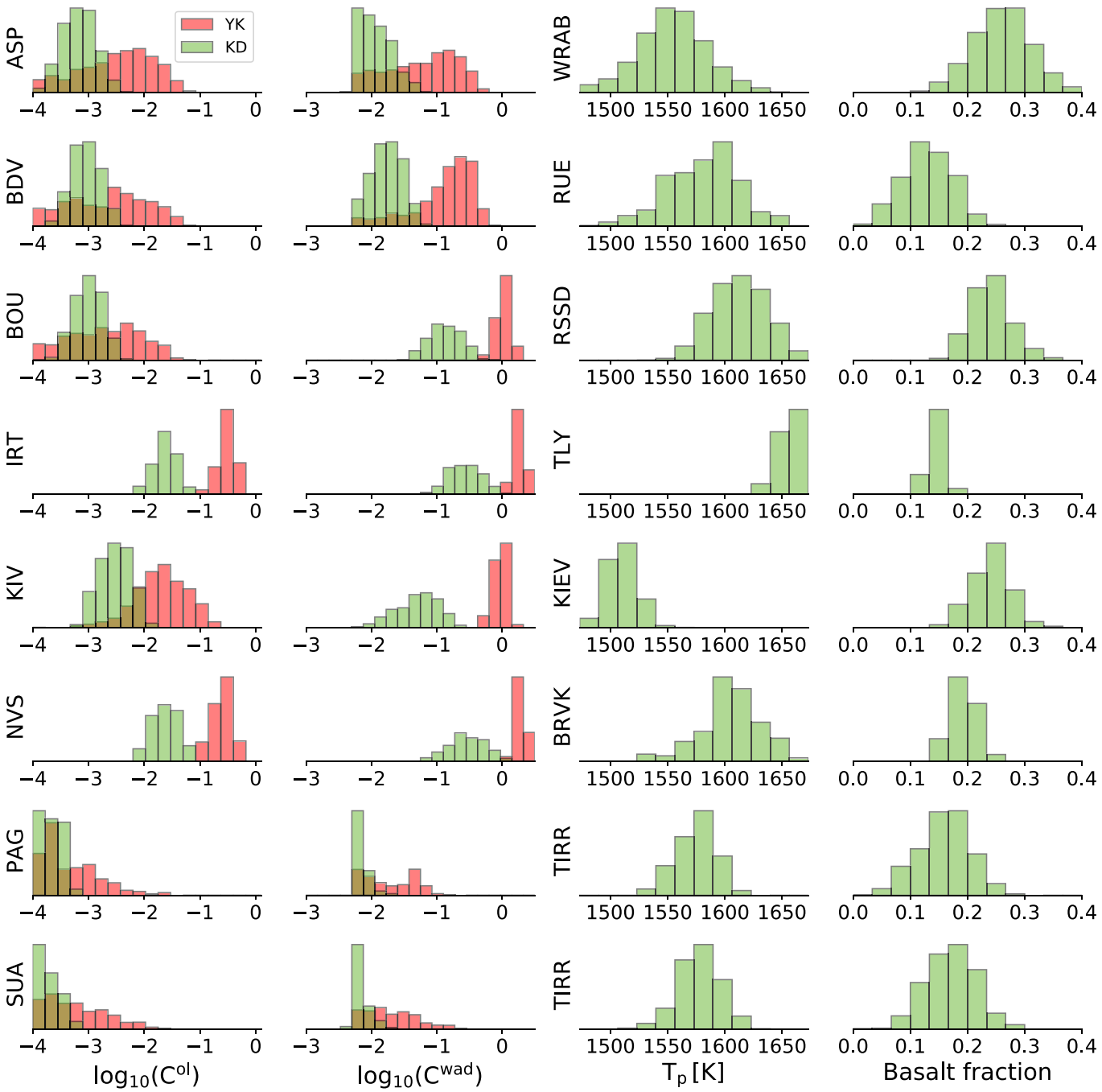

Figure 4. Sampled water content in (a) olivine and (b) wadsleyite retrieved using the Yoshino-Katsura (YK) and Karato-Dai (KD) electrical conductivity databases. Water contents are given in terms of $C^x = C^x_w / C^x_w$, where x denotes either of the minerals olivine and wadsleyite, C^x_w is inwt%, and $C^0_w = 1$ wt%. Constraints on the probability distribution of (c) mantle potential temperature (T_p) and (d) composition (basalt fraction) were obtained from the inversion of P-to-s receiver functions and Rayleigh wave phase velocities (Munch et al., 2020). Station acronyms are defined in Table S1, and geographic locations are depicted in Figure 2.

the near-water saturated conditions implied by hydrous ringwoodite inclusions found in a natural diamond (Pearson et al., 2014) are not representative of the whole MTZ.

4. Conclusions

In this study, we combined EM responses in a wide period band to infer the electrical conductivity structure underneath a set of inland geomagnetic observatories, while accounting for complex spatial structure of the

magnetospheric and ionospheric sources (Püthe et al., 2015b). We found that simplistic source models are likely to introduce significant errors in the estimated TFs and therefore bias the inferred conductivity models. Furthermore, the incorporation of daily band responses (6–24 hr) into the inversion leads to improved model resolution, especially in the upper mantle and MTZ.

The retrieved conductivity models were subsequently interpreted in terms of variations in upper mantle (olivine) and transition zone (wadsleyite) water content by combining mineral phase equilibria calculations, laboratory-based electrical conductivity measurements, and estimates on mantle temperature and major element chemistry derived independently from the inversion of short- and long-period seismic data. We find the existence of a relatively dry transition zone beneath Europe (C_w^{wad} <0.05 wt%) and a water-enriched ($C_w^{\mathrm{wad}} \sim 0.3$ wt%) transition zone underneath North America and northern Asia. These findings suggest that the near-water saturated conditions hinted at by hydrous ringwoodite inclusions found in a natural diamond (Pearson et al., 2014) are not likely to be representative of the entire MTZ.

The methodology presented here provides quantitative constraints on water content in the upper mantle and MTZ. To move beyond the current results and improve our understanding of the water distribution in the deep mantle and mantle water circulation, future work should aim at (1) extending the geographical distribution of geomagnetic observatories to include data from coastal and island and (2) inverting EM and seismic data jointly by means of an integrated approach (e.g., Khan, 2016). The former demands the use of 3-D EM solvers to account for the ocean induction effect (e.g., Kuvshinov et al., 2002), which makes the implementation of Markov chain Monte Carlo methods impracticable. The latter requires a refinement of the laboratory-based electrical conductivity databases to lower-mantle minerals, and the extension of the thermodynamic database employed for mineral phase equilibria calculations to account for effects related to oxygen fugacity, water content, and melt.

Appendix A: Estimation of Magnetospheric Source Coefficients

Maxwell's equations describe the spatiotemporal behavior of electormagnetic (EM) fields and can be formulated in frequency domain as

$$\frac{1}{\mu_0}\nabla \times \mathbf{B}(\mathbf{r},\omega) = \sigma(\mathbf{r})\mathbf{E}(\mathbf{r},\boldsymbol{\omega}) + \mathbf{j}^{\mathrm{ext}}(\mathbf{r},\omega), \tag{A1}$$

$$\nabla \times \mathbf{E}(\mathbf{r},\omega) = i\omega\mathbf{B}(\mathbf{r},\omega), \tag{A2}$$

where $\mathbf{B}$ and $\mathbf{E}$ represent the complex Fourier transforms of magnetic flux density and electric field at a location $\mathbf{r} = (r, \vartheta, \varphi)$. The distance from the Earth's center is denoted by r, ϑ is the colatitude, and φ is the longitude. Furthermore, $\mathbf{j}^{\mathrm{ext}}(\mathbf{r},\omega)$ is the complex Fourier transform of an impressed source current density, $\sigma(\mathbf{r})$ represents the electrical conductivity distribution in the media, ω is the angular frequency, and μ_0 is the magnetic permeability of free space. Given that deep EM studies consider induction due to natural current systems that vary on timescales between a few hours and a few months, displacement currents are here neglected.

Above the conducting Earth and below the region enclosed by the current $\mathbf{j}^{\mathrm{ext}}$, equation (A1) reduces to $\nabla \times \mathbf{B} = 0$; thus, $\mathbf{B}$ is a potential field that can be described as a gradient of a scalar potential V

$$\mathbf{B} = -\nabla V. \tag{A3}$$

Since$\nabla \cdot \mathbf{B} = 0$, then V satisfies Laplace's equation ($\nabla^2 V = 0$) and hence can be decomposed into external and internal parts such that $V = V^{\mathrm{ext}} + V^{\mathrm{int}}$, where

$$V^{\mathrm{ext}} = a\sum_{n=1}^{N_\varepsilon}\sum_{m=-n}^{n}\varepsilon_n^m(\omega)\left(\frac{r}{a}\right)^n Y_n^m(\vartheta,\varphi), \tag{A4}$$

$$V^{\text{int}} = a\sum_{k=1}^{N_\iota}\sum_{l=-k}^{k} \iota_k^l(\omega)\left(\frac{r}{a}\right)^{-(k+1)} Y_k^l(\vartheta,\varphi), \tag{A5}$$

where $\epsilon_n^m(\omega)$ and $\iota_k^l(\omega)$ are the spherical harmonic expansion (SHE) coefficients of the external (inducing) and internal (induced) parts of the potential, N_ϵ and N_ι are the maximum (cutoff) degrees for external and internal coefficients, respectively, and Y_n^m is the spherical harmonic of degree n and order m

$$Y_n^m(\vartheta,\varphi) = P_n^{|m|}(\cos\vartheta)e^{im\varphi}, \tag{A6}$$

where $P_n^{|m|}(\cos\vartheta)$ corresponds to the Schmidt quasinormalized associated Legendre function of degree n and order $|m|$. Note that in equations (A4) and (A5), we use different indices for external and internal coefficients to account for the 3-D conductivity distribution. In a 1-D Earth (in which conductivity is only a function of depth), every external coefficient only induces one internal coefficient of the same degree and order. They are linearly related by the (scalar) Q-response, which is defined as

$$\iota_n^m(\omega) = Q_n(\omega)\epsilon_n^m(\omega). \tag{A7}$$

Note that in 1-D case, Q_n is independent of the order m (e.g., Bailey, 1969) and $N_\epsilon = N_\iota$. In a 3-D Earth, however, every external coefficient ϵ_n^m induces a whole series of internal coefficients ι_k^l such that we can write

$$\iota_k^l(\omega) = \sum_{n=1}^{N_\epsilon}\sum_{m=-n}^{n} Q_{kn}^{lm}(\omega)\epsilon_n^m(\omega), \tag{A8}$$

where the Q_{kn}^{lm} form a 2-D array of transfer functions (TFs) we refer to as Q-matrix. The diagonal elements of this matrix mostly describe the bulk conductivity, and, in case of a layered (1-D) Earth, they are equivalent to the scalar Q-responses. The off-diagonal elements describe a transfer of energy to coefficients of different degree and order, which only occurs if the subsurface has a 3-D structure. Note that our a priori 3-D Earth's model consists of a mantle with 1-D conductivity distribution overlaid by a surface layer of known laterally variable conductance; the latter approximates nonuniform distribution of oceans and continents. Our numerical experiments shows that the diagonal elements of corresponding Q-matrix are dominant for the considered period range (3–85 days). Therefore, exploiting equations (A3)–(A5) and (A8), the magnetic field on the surface of the Earth, $\mathbf{r}_a = (a,\vartheta,\varphi)$, can be written as

$$B_r(\mathbf{r}_a,\omega) = -\sum_{n=1}^{N_\epsilon}\sum_{m=-n}^{n} \epsilon_n^m(\omega)\left[n-(n+1)Q_{nn}^{mm}(\omega)\right]Y_n^m(\vartheta,\varphi), \tag{A9}$$

$$\mathbf{B}_\tau(\mathbf{r}_a,\omega) = -\sum_{n=1}^{N_\epsilon}\sum_{m=-n}^{n} \epsilon_n^m(\omega)\left[1+Q_{nn}^{mm}(\omega)\right]\nabla_\perp Y_n^m(\vartheta,\varphi), \tag{A10}$$

where subscriptτ denotes the tangential part of $\mathbf{B}$ and $\nabla_\perp$ is the surface gradient. With the following denotation

$$\nu_n^m(\omega) = \epsilon_n^m(\omega)\left[1+Q_{nn}^{mm}(\omega)\right], \tag{A11}$$

time domain equivalent of equation (A10) reads

$$\mathbf{B}_\tau(\mathbf{r}_a,t) = -\sum_{n=1}^{N_\epsilon}\sum_{m=-n}^{n} \nu_n^m(t)\nabla_\perp Y_n^m(\vartheta,\varphi). \tag{A12}$$

In this study, we estimated external source coefficients $\epsilon_n^m(t)$ following the procedure proposed by Püthe et al. (2015b). This procedure can be summarized as follows:

1. Collection of hourly mean time series of geomagnetic field components from midlatitude permanent observatories (see Figure S1) from the British Geological Survey database (Macmillan & Olsen, 2013).
2. Removal of the main field and its secular variations using the CHAOS model (Olsen et al., 2006).
3. Detrend each magnetic field component using cubic B-splines.
4. Rotation of the horizontal magnetic field components from geographic to geomagnetic coordinates using geomagnetic north pole coordinates for the year 2010.

5. Estimation of v_n^m for each time instant t from the tangential components of the observed magnetic field in geomagnetic coordinates using equation (A12) and a Huber-weighted robust least squares method (e.g., Aster et al., 2005). Weights are meant to counteract potential biases introduced by cluster of stations (e.g., the high concentrations of observatories in the Northern Hemisphere). At each time instant t, we triangulate the spatial distribution of observatories (via calculating the convex hull). Weights are then estimated as the surface area of the spherical triangle that has a given observatory as its center.
6. Separation of internal and external contributions as follows:
   a. Transformation of the unseparated coefficients $v_n^m(t)$ into frequency domain.
   b. Computation of radial magnetic field $B_{n,r}^m(\mathbf{r}_a, \omega)$ induced by unit amplitude spherical harmonic sources ($\epsilon_n^m = 1$) in frequency domain using a numerical solver based on integral equation approach (Kuvshinov, 2008). As mentioned above, computations are performed in a priori 3-D Earth's model consisting of a mantle with 1-D conductivity distribution overlaid by a surface layer of laterally variable conductance.
   c. Calculation of $Q_{nn}^{mm}(\omega)$ from the computed $B_{n,r}^m(\mathbf{r}_a, \omega)$ as (Püthe & Kuvshinov, 2014)

$$Q_{nn}^{mm}(\omega) = \frac{1}{(n+1)||Y_n^m||^2} \int_\Omega \left[B_{n,r}^m(\mathbf{r}_a, \omega) - B_{n,r}^{m,\text{ext}}(\mathbf{r}_a) \right] \hat{Y}_n^m(\vartheta, \varphi) ds. \tag{A13}$$

   Here, $\hat{Y}_n^m$ denotes complex conjugation Y_n^m, Ω is the complete solid angle, $ds = \sin\vartheta d\vartheta d\varphi$, and $||Y_n^m||^2$ is the squared norm of the spherical harmonic Y_n^m, and $B_{n,r}^{m,\text{ext}}$ is the external part of radial magnetic field, that is,

$$B_{n,r}^{m,\text{ext}}(\mathbf{r}_a) = -nY_n^m(\vartheta, \varphi). \tag{A14}$$

   Substituting equation (A14) into equation (A13), we have

$$Q_{nn}^{mm}(\omega) = \frac{1}{(n+1)||Y_n^m||^2} \int_\Omega B_{n,r}^m(\mathbf{r}_a, \omega) \hat{Y}_n^m(\vartheta, \varphi) ds + \frac{n}{n+1}. \tag{A15}$$

   d. Separation of internal and external contributions using equation (A11)

$$\epsilon_n^m(\omega) = v_n^m(\omega)/[1 + Q_{nn}^{mm}(\omega)].$$

   e. Transformation of the external coefficients $\epsilon_n^m(\omega)$ into time domain.

Acknowledgments
We are grateful to two anonymous reviewers for their constructive comments, which helped improve the manuscript. F. D. M. was supported by a grant from the Swiss National Science Foundation (Project No. 159907). A. V. G. and A. V. K. were supported by the European Space Agency through the Swarm DISC project. M. G. was supported by ETH Zürich Grant ETH-3215-2. The authors would also like to acknowledge the British Geological Survey (BGS), WDC Geomagnetism (Edinburgh), INTERMAGNET, and the many institutes around the world that operate magnetic observatories. Time series of geomagnetic field components used in this study are available on ftp://ftp.nerc-murchison.ac.uk/geomag/Swarm/AUX_OBS/hour. Long-period transfer functions and main inversion results (conductivity profiles, water content, basalt fraction, and mantle potential temperature estimates) for each stations are available on the website (https://doi.org/10.3929/ethz-b-000405622).

References

Aster, R., Borchers, B., & Thurber, C. (2005). *Parameter estimation and inverse problems*. Amsterdam: Elsevier academic.
Bahr, K., Olsen, N., & Shankland, T. J. (1993). On the combination of the magnetotelluric and the geomagnetic depth sounding method for resolving an electrical conductivity increase at 400 km depth. *Geophysical Research Letters*, *20*(24), 2937–2940.
Bailey, R. (1969). Inversion of the geomagnetic induction problem. *Proceedings of the Royal Society*, *315*, 185–194.
Balasis, G., & Egbert, G. D. (2006). Empirical orthogonal function analysis of magnetic observatory data: Further evidence for non-axisymmetric magnetospheric sources for satellite induction studies. *Geophysical Research Letters*, *33*, L11311. https://doi.org/10.1029/2006GL025721
Banks, R. (1969). Geomagnetic variations and the electrical conductivity of the upper mantle. *Geophysical Journal International*, *17*(5), 457–487.
Bercovici, D., & Karato, S.-i. (2003). Whole-mantle convection and the transition-zone water filter. *Nature*, *425*(6953), 39–44.
Bolfan-Casanova, N. (2005). Water in the Earth's mantle. *Mineralogical Magazine*, *69*(3), 229–257.
Bolfan-Casanova, N., Mccammon, C. A., & Mackwell, S. J. (2006). Water in transition zone and lower mantle minerals. *Geophysical Monograph-American Geophysical Union*, *168*, 57.
Connolly, J. (2009). The geodynamic equation of state: What and how. *Geochemistry, Geophysics, Geosystems*, *10*, Q10014. https://doi.org/10.1029/2009GC002540
Cottaar, S., & Deuss, A. (2016). Large-scale mantle discontinuity topography beneath Europe: Signature of akimotoite in subducting slabs. *Journal of Geophysical Research: Solid Earth*, *121*, 279–292. https://doi.org/10.1002/2015JB012452
Daglis, I., & Kozyra, J. (2002). Outstanding issues of ring current dynamics. *Journal of Atmospheric and Solar-Terrestrial Physics*, *64*(2), 253–264.
Egbert, G. D., & Booker, J. R. (1992). Very long period magnetotellurics at Tucson observatory: Implications for mantle conductivity. *Journal of Geophysical Research*, *97*(B11), 15,099–15,112.
Ferot, A., & Bolfan-Casanova, N. (2012). Water storage capacity in olivine and pyroxene to 14 GPa: Implications for the water content of the Earth's upper mantle and nature of seismic discontinuities. *Earth and Planetary Science Letters*, *349*, 218–230.
Finlay, C., Lesur, V., Thébault, E., Vervelidou, F., Morschhauser, A., & Shore, R. (2017). Challenges handling magnetospheric and ionospheric signals in internal geomagnetic field modelling.
Freitas, D., Manthilake, G., Schiavi, F., Chantel, J., Bolfan-Casanova, N., Bouhifd, M., & Andrault, D. (2017). Experimental evidence supporting a global melt layer at the base of the Earth's upper mantle. *Nature Communications*, *8*(1), 2186.

Fullea, J., Muller, M., & Jones, A. (2011). Electrical conductivity of continental lithospheric mantle from integrated geophysical and petrological modeling: Application to the Kaapvaal Craton and Rehoboth Terrane, southern Africa. *Journal of Geophysical Research*, *116*, B10202. https://doi.org/10.1029/2011JB008544

Grayver, A. V., & Kuvshinov, A. V. (2016). Exploring equivalence domain in nonlinear inverse problems using Covariance Matrix Adaption Evolution Strategy (CMAES) and random sampling. *Geophysical Journal International*, *205*(2), 971–987.

Grayver, A., Munch, F., Kuvshinov, A., Khan, A., Sabaka, T., & Tøffner-Clausen, L. (2017). Joint inversion of satellite-detected tidal and magnetospheric signals constrains electrical conductivity and water content of the upper mantle and transition zone. *Geophysical Research Letters*, *44*, 6074–6081. https://doi.org/10.1002/2017GL073446

Guzavina, M., Grayver, A., & Kuvshinov, A. (2019). Probing upper mantle electrical conductivity with daily magnetic variations using global-to-local transfer functions. *Geophysical Journal International*, *219*(3), 2125–2147.

Hansen, P. C. (1999). The L-curve and its use in the numerical treatment of inverse problems.

Hansen, N., & Ostermeier, A. (2001). Completely derandomized self-adaptation in evolution strategies. *Evolutionary Computation*, *9*(2), 159–195.

Hastings, W. K. (1970). Monte Carlo sampling methods using Markov chains and their applications. *Biometrika*, *57*(1), 97–109.

Hirschmann, M. M. (2006). Water, melting, and the deep Earth H_2O cycle. *Annual Review of Earth and Planetary Sciences*, *34*, 629–653.

Hirschmann, M. M., Aubaud, C., & Withers, A. C. (2005). Storage capacity of H_2O in nominally anhydrous minerals in the upper mantle. *Earth and Planetary Science Letters*, *236*(1), 167–181.

Inoue, T., Wada, T., Sasaki, R., & Yurimoto, H. (2010). Water partitioning in the Earth's mantle. *Physics of the Earth and Planetary Interiors*, *183*(1), 245–251.

Jones, A. G., Fullea, J., Evans, R. L., & Muller, M. R. (2012). Water in cratonic lithosphere: Calibrating laboratory-determined models of electrical conductivity of mantle minerals using geophysical and petrological observations. *Geochemistry, Geophysics, Geosystems*, *13*, Q06010. https://doi.org/10.1029/2012GC004055

Karato, S.-i. (2011). Water distribution across the mantle transition zone and its implications for global material circulation. *Earth and Planetary Science Letters*, *301*(3), 413–423.

Katsura, T., & Yoshino, T. (2015). Heterogeneity of electrical conductivity in the oceanic upper mantle. In *The Earth's heterogeneous mantle*. Cham: Springer.

Kelbert, A., Schultz, A., & Egbert, G. (2009). Global electromagnetic induction constraints on transition-zone water content variations. *Nature*, *460*(7258), 1003–1006.

Khan, A. (2016). On Earth's mantle constitution and structure from joint analysis of geophysical and laboratory-based data: An example. *Surveys in Geophysics*, *37*(1), 149–189.

Khan, A., & Shankland, T. (2012). A geophysical perspective on mantle water content and melting: Inverting electromagnetic sounding data using laboratory-based electrical conductivity profiles. *Earth and Planetary Science Letters*, *317*, 27–43.

Koch, S., & Kuvshinov, A. (2013). Global 3-D EM inversion of Sq variations based on simultaneous source and conductivity determination: Concept validation and resolution studies. *Geophysical Journal International*, *195*(1), 98–116.

Koyama, T., Khan, A., & Kuvshinov, A. (2014). Three-dimensional electrical conductivity structure beneath Australia from inversion of geomagnetic observatory data: Evidence for lateral variations in transition-zone temperature, water content and melt. *Geophysical Journal International*, *196*(3), 1330.

Koyama, T., Shimizu, H., Utada, H., Ichiki, M., Ohtani, E., & Hae, R. (2006). Water content in the mantle transition zone beneath the North Pacific derived from the electrical conductivity anomaly. *Earth's Deep Water Cycle*, *168*, 171–179.

Kuvshinov, A. (2008). 3-D global induction in the oceans and solid Earth: Recent progress in modeling magnetic and electric fields from sources of magnetospheric, ionospheric and oceanic origin. *Surveys in Geophysics*, *29*(2), 139–186.

Kuvshinov, A. V., Olsen, N., Avdeev, D. B., & Pankratov, O. V. (2002). Electromagnetic induction in the oceans and the anomalous behaviour of coastal *C*-responses for periods up to 20 days. *Geophysical Research Letters*, *29*(12), 36–1-36-4.

Litasov, K. D., Shatskiy, A., Ohtani, E., & Katsura, T. (2011). Systematic study of hydrogen incorporation into Fe-free wadsleyite. *Physics and Chemistry of Minerals*, *38*(1), 75–84.

Macmillan, S., & Olsen, N. (2013). Observatory data and the Swarm mission. *Earth, Planets and Space*, *65*(11), 1355–1362.

McKenzie, D., & Bickle, M. (1988). The volume and composition of melt generated by extension of the lithosphere. *Journal of Petrology*, *29*(3), 625–679.

Metropolis, N., Rosenbluth, A. W., Rosenbluth, M. N., Teller, A. H., & Teller, E. (1953). Equation of state calculations by fast computing machines. *The Journal of Chemical Physics*, *21*(6), 1087–1092.

Mookherjee, M., & Karato, S.-i. (2010). Solubility of water in pyrope-rich garnet at high pressures and temperature. *Geophysical Research Letters*, *37*, L03310. https://doi.org/10.1029/2009GL041289

Mosegaard, K., & Tarantola, A. (1995). Monte Carlo sampling of solutions to inverse problems. *Journal of Geophysical Research*, *100*(B7), 12,431–12,447.

Munch, F., Grayver, A., Kuvshinov, A., & Khan, A. (2018). Stochastic inversion of geomagnetic observatory data including rigorous treatment of the ocean induction effect with implications for transition zone water content and thermal structure. *Journal of Geophysical Research: Solid Earth*, *123*, 31–51. https://doi.org/10.1002/2017JB014691

Munch, F., Khan, A., Tauzin, B., van Driel, M., & Giardini, D. (2020). Seismological evidence for thermo-chemical heterogeneity in Earth's continental mantle. *Earth and Planetary Science Letters*, *539*, 116240. https://doi.org/10.1016/j.epsl.2020.116240

Ohtani, E., Litasov, K., Hosoya, T., Kubo, T., & Kondo, T. (2004). Water transport into the deep mantle and formation of a hydrous transition zone. *Physics of the Earth and Planetary Interiors*, *143*, 255–269.

Olsen, N. (1998). The electrical conductivity of the mantle beneath Europe derived from *C*-responses from 3 to 720 hr. *Geophysical Journal International*, *133*(2), 298–308.

Olsen, N., & Kuvshinov, A. (2004). Modeling the ocean effect of geomagnetic storms. *Earth, Planets and Space*, *56*(5), 525–530.

Olsen, N., Lühr, H., Sabaka, T. J., Mandea, M., Rother, M., Tøffner-clausen, L., & Choi, S. (2006). CH,AOS—A model of the Earth's magnetic field derived from CHAMP, Ørsted, and SAC-C magnetic satellite data. *Geophysical Journal International*, *166*(1), 67–75.

Olsen, N., & Stolle, C. (2017). Magnetic signatures of ionospheric and magnetospheric current systems during geomagnetic quiet conditions—An overview. *Space Science Reviews*, *206*(1-4), 5–25.

Pearson, D., Brenker, F., Nestola, F., McNeill, J., Nasdala, L., Hutchison, M., et al. (2014). Hydrous mantle transition zone indicated by ringwoodite included within diamond. *Nature*, *507*(7491), 221.

Peslier, A. H., & Bizimis, M. (2015). Water in Hawaiian peridotite minerals: A case for a dry metasomatized oceanic mantle lithosphere. *Geochemistry, Geophysics, Geosystems*, *16*, 1211–1232. https://doi.org/10.1002/2015GC005780

Peslier, A. H., Woodland, A. B., Bell, D. R., & Lazarov, M. (2010). Olivine water contents in the continental lithosphere and the longevity of cratons. *Nature*, *467*(7311), 78.

Püthe, C., & Kuvshinov, A. (2014). Mapping 3-D mantle electrical conductivity from space: A new 3-D inversion scheme based on analysis of matrix *Q*-responses. *Geophysical Journal International*, *197*(2), 768–784.

Püthe, C., Kuvshinov, A., Khan, A., & Olsen, N. (2015a). A new model of Earth's radial conductivity structure derived from over 10 yr of satellite and observatory magnetic data. *Geophysical Journal International*, *203*(3), 1864–1872.

Püthe, C., Kuvshinov, A., & Olsen, N. (2015b). Handling complex source structures in global EM induction studies: From *C*-responses to new arrays of transfer functions. *Geophysical Journal International*, *201*(1), 318–328.

Semenov, A., & Kuvshinov, A. (2012). Global 3-D imaging of mantle conductivity based on inversion of observatory *C*-responses—II. Data analysis and results. *Geophysical Journal International*, *191*(3), 965–992.

Shimizu, H., Utada, H., Baba, K., Koyama, T., Obayashi, M., & Fukao, Y. (2010). Three-dimensional imaging of electrical conductivity in the mantle transition zone beneath the North Pacific Ocean by a semi-global induction study. *Physics of the Earth and Planetary Interiors*, *183*(1), 252–269.

Stixrude, L., & Lithgow-Bertelloni, C. (2005). Thermodynamics of mantle minerals—I. Physical properties. *Geophysical Journal International*, *162*(2), 610–632.

Stixrude, L., & Lithgow-Bertelloni, C. (2011). Thermodynamics of mantle minerals—II. Phase equilibria. *Geophysical Journal International*, *184*(3), 1180–1213.

Sun, J., Kelbert, A., & Egbert, G. (2015). Ionospheric current source modeling and global geomagnetic induction using ground geomagnetic observatory data. *Journal of Geophysical Research: Solid Earth*, *120*, 6771–6796. https://doi.org/10.1002/2015JB012063

Tarantola, A., & Valette, B. (1982). Generalized nonlinear inverse problems solved using the least squares criterion. *Reviews of Geophysics*, *20*(2), 219–232.

Utada, H., Koyama, T., Obayashi, M., & Fukao, Y. (2009). A joint interpretation of electromagnetic and seismic tomography models suggests the mantle transition zone below Europe is dry. *Earth and Planetary Science Letters*, *281*(3), 249–257.

Yamazaki, Y., & Maute, A. (2017). Sq and EEJ—A review on the daily variation of the geomagnetic field caused by ionospheric dynamo currents. *Space Science Reviews*, *206*(1-4), 299–405.

Zhu, H., Bozdağ, E., & Tromp, J. (2015). Seismic structure of the European upper mantle based on adjoint tomography. *Geophysical Journal International*, *201*(1), 18–52.